mathematics

MDPI

Article

The Control Mechanism of the Coal Pillar Width on the Mechanical State of Hard Roofs

Qifeng Jia [1,2], Songtao Ji [1,*], Jie Zhang [3], Zhiyu Fang [1], Chao Lyu [1] and Jurij Karlovšek [4]

[1] College of Energy and Mining Engineering, Xi'an University of Science and Technology, Xi'an 710054, China; qfjia@xust.edu.cn (Q.J.); fangzy@stu.xust.edu.cn (Z.F.); lvchao@cumt.edu.cn (C.L.)
[2] State and Local Joint Engineering Laboratory for Gas Drainage & Ground Control of Deep Mines, Henan Polytechnic University, Jiaozuo 454099, China
[3] College of Safety Science and Engineering, Xi'an University of Science and Technology, Xi'an 710054, China; jie.zhang@xust.edu.cn
[4] School of Civil Engineering, The University of Queensland, Brisbane, QLD 4067, Australia; j.karlovsek@uq.edu.au
* Correspondence: songtao.ji@xust.edu.cn

Abstract

This study addresses the critical challenge of optimizing coal pillar width in burst-prone mines with thick, hard roof strata, balancing resource recovery, roadway stability, and coal burst mitigation. Through integrated analytical modeling and rigorously calibrated numerical simulations, the research reveals the complex interplay between pillar width, roof mechanics, and stress redistribution. Key findings demonstrate that pillar width dictates roof failure mechanics and energy accumulation. The case study indicates that increasing the coal pillar width from 6 m to 20 m shifts the tensile fracture location from solid coal toward the pillar center, migrates shear failure zones closer to roadways, and relocates elastic strain energy accumulation to the pillar area. This concentrates static and dynamic loads directly onto wider pillars upon roof fracture, escalating instability risks. A risky coal pillar width is identified as 10–20 m, where pillars develop severe lateral abutment pressures perilously close to roadways, combining high elastic energy storage with exposure to roof fracture dynamics. Conversely, narrow pillars exhibit low stress concentrations and limited energy storage due to plastic deformation, reducing burst potential despite requiring robust asymmetric support. Strategic selection of narrow or wide pillars provides a safer pathway. The validated analytical–numerical framework offers a scientifically grounded methodology for pillar design under hard roof conditions, enhancing resource recovery while mitigating coal burst risks.

Keywords: coal pillar width; hard roof; ground control; abutment stress; numerical simulation

MSC: 74-10

check for updates

Academic Editor: Smirnov Nikolay Nikolaevich

Received: 22 July 2025
Revised: 7 August 2025
Accepted: 7 August 2025
Published: 8 August 2025

Citation: Jia, Q.; Ji, S.; Zhang, J.; Fang, Z.; Lyu, C.; Karlovšek, J. The Control Mechanism of the Coal Pillar Width on the Mechanical State of Hard Roofs. *Mathematics* **2025**, *13*, 2548. https://doi.org/10.3390/math13162548

Copyright: © 2025 by the authors. Licensee MDPI, Basel, Switzerland. This article is an open access article distributed under the terms and conditions of the Creative Commons Attribution (CC BY) license (https://creativecommons.org/licenses/by/4.0/).

1. Introduction

The strategic implementation of narrow or even no-coal-pillar layouts has gained significant traction in modern underground coal mining. This paradigm shift is fundamentally driven by the imperative to maximize resource recovery rates, minimizing valuable coal left trapped within inter-panel barriers. Furthermore, in burst-prone mining environments, appropriately sized pillars can serve as critical energy absorbers and stress regulators, potentially mitigating the catastrophic risk of coal burst events by preventing excessive stress

concentration within the surrounding rock mass [1,2]. However, this drive towards reduced pillar dimensions presents a profound and complex engineering challenge: excessively narrow pillars inherently compromise their load-bearing capacity and stability [3]. Such compromised pillars become vulnerable to excessive deformation, crushing, or catastrophic failure, directly jeopardizing the integrity of adjacent roadways, increasing ground control costs, and posing severe safety hazards to personnel and equipment. Despite decades of research and practical application, the determination of a universally applicable or consistently reliable coal pillar width, particularly under the demanding conditions of hard roof strata and burst-prone seams, remains an elusive goal, lacking a definitive theoretical or empirical foundation [4,5]. The selection process often involves navigating a precarious balance between competing objectives of resource conservation, operational safety, and economic viability.

Field observations and monitoring data consistently underscore that the stability and performance of narrow coal pillars are not governed by width alone but are profoundly sensitive to the intricate interplay of site-specific geological and operational factors. Crucially, the nature of the immediate roof and floor strata exerts a dominant influence; the presence of massive, competent, and hard roof formations significantly alters the overburden load transfer mechanics and the dynamic behavior of the strata surrounding the pillar [6,7]. Under such conditions, hard roofs tend to form large, cantilevered structures or voussoir beams, imposing substantial and often asymmetrical abutment pressures onto the underlying pillars. Concurrently, the inherent mechanical properties of the coal seam itself, such as the uniaxial compressive strength, modulus, brittleness, and presence of natural discontinuities, dictate the pillar's intrinsic resistance to deformation and failure [8]. Equally critical is the design and efficacy of the support system installed within the adjacent roadway; inadequate or poorly configured support cannot compensate for an inherently unstable pillar, while effective support can enhance pillar confinement and overall system stability [9,10]. Consequently, there exists a compelling necessity for systematic, integrated research focused explicitly on determining rational coal pillar dimensions within the high-risk context of burst-prone coal mines characterized by thick, hard roof strata [11,12]. Understanding the unique mechanics of this geological setting is paramount for developing safe and efficient pillar design methodologies.

Significant research efforts have been dedicated to developing analytical frameworks and monitoring techniques for understanding coal pillar behavior and sizing. Conventional deterministic approaches, often based on limit equilibrium theory and empirical strength formulas, provide simplicity but struggle to account for inherent uncertainties in material properties and complex loading scenarios arising from mining activities [13,14]. Probabilistic methods, such as the First-Order Second Moment and Advanced Second Moment techniques, have been employed to quantify the reliability and confidence intervals of pillar stability, acknowledging the stochastic nature of input parameters like coal strength and abutment pressure [5]. Studies applying these methods demonstrated confidence intervals for pillar stability ranging from 84% to 88% under specific conditions, highlighting the inherent variability that deterministic methods overlook. Elastic and elastoplastic theoretical models have been formulated to calculate stress distributions within pillars, identify the extent of limit equilibrium zones prone to yielding, and determine the necessary width for maintaining a stable elastic core [15–17]. Research indicates that the width of the limit equilibrium zone is inversely related to the ultimate tensile strain and elastic modulus of the coal–rock mass, while positively correlating with mining depth and pillar height [18]. Furthermore, advanced field monitoring techniques like active seismic tomography have been successfully employed to image stress redistribution within yield pillars during longwall retreat [19]. The critical width required to develop a protective elastic core is influenced

by factors like the friction angle at the coal/roof/floor interface and pillar geometry. These analytical approaches provide essential fundamental insights into the stress state and failure mechanics governing pillar stability.

Numerical modeling, encompassing techniques like Finite Difference Method (FLAC3D), Finite Element Method (FEM), and Discrete Element Method (DEM), has become indispensable for simulating the complex response of coal pillars and surrounding strata under various widths and loading conditions [20]. These simulations effectively visualize stress evolution, displacement patterns, and plastic zone development, providing a detailed mechanistic understanding. Studies consistently reveal that pillar stress distribution and the morphology of the failure zone are highly sensitive to pillar width [21]. Narrow pillars often exhibit asymmetric deformation and stress concentrations, particularly near acute corners in non-rectangular geometries, and may experience significant crushing or shear failure, especially under dynamic loading or in the presence of geological discontinuities [4]. Field investigations employing techniques like borehole stress monitoring, convergence measurement, and seismic tomography have validated model predictions, showing that mining-induced stress can reach 2–3 times the in situ stress, with peak stresses often located deep within the pillar [22]. Crucially, research has identified distinct failure modes: narrow pillars often fail due to insufficient strength to resist high abutment pressures, experiencing large, asymmetric deformations [23,24]. Wider pillars may avoid catastrophic failure but can still develop large plastic zones, transferring high stresses into adjacent roadways and virgin coal. Optimal widths, often identified in the range of 6–15 m depending on seam thickness and depth, aim to position the roadway within a lower stress environment, balance high- and low-strength-bearing zones within the pillar, and ensure a sufficiently large, stable elastic core [24]. The detrimental effects of time-dependent pillar scaling, progressively reducing effective width and strength, have also been quantified, emphasizing the need for designs incorporating long-term stability [2].

Research underscores that rational pillar design cannot be divorced from the specific geological context and employed mining methodology. The thickness and inclination of the coal seam fundamentally alter pillar behavior; thick seams necessitate taller pillars, increasing the risk of buckling and reducing strength-to-weight ratios, while inclined seams introduce complex shear components and asymmetric loading [25]. The presence of a hard, thick main roof significantly increases the load transferred onto pillars and influences fracture development and strata behavior above the goaf, often dictating larger pillar requirements or specialized support [6]. Multi-seam mining scenarios, particularly where lower seams are extracted beneath residual coal pillars from upper seams, create highly irregular and elevated stress fields, demanding careful pillar placement and width selection to avoid instability [7]. The chosen mining method directly impacts the magnitude and distribution of abutment pressures acting on the pillars. Backfilling has been explored as a method to enhance pillar confinement and potentially allow for narrower pillars by providing lateral support and reducing load [11,26]. Complementing pillar width optimization, tailored support strategies are paramount. Studies advocate for asymmetric support systems in roadways adjacent to narrow pillars to counteract uneven loads, employing techniques like roof bolting, cable bolting, mesh, and strategic grouting to reinforce the pillar ribs, control fractured zones, and enhance the overall bearing capacity of the pillar–roadway system. The concept of forming a “cooperative bearing system” between the support and the surrounding rock, adapting to the specific stress environment induced by the pillar width, is critical for successful ground control.

Despite progress in pillar design, a key gap remains in understanding how coal pillar width interacts with stress evolution and hard roof mechanics in burst-prone mines. Existing studies often examine pillar stress or roof behavior separately, lacking resolution

to capture the mechanical behavior of hard roofs and coal pillars under high-stress conditions. Specifically, failure mechanisms and stability thresholds for pillars under hard roofs are quantified. This study bridges this gap by combining analytical modeling with PFC (Particle Flow Code)–FLAC (Fast Lagrangian Analysis of Continua) coupled simulations. It models pillar–roof interactions across varying widths, analyzing stress redistribution, deformation, fracture development, and energy evolution. The primary objective is to establish a methodology for determining rational coal pillar widths that simultaneously ensure roadway stability, mitigate coal burst risks, and optimize resource recovery under these geotechnically challenging conditions.

2. Mechanical Model of Coal Pillar

The deformation movement of the roof along the working face can be regarded as a plane strain problem. Taking the coal rock layer per unit width of the working face as the research object, the hard roof is simplified as a rock beam model for study. According to the different foundation support conditions of the roof, it can be divided into 5 parts, as shown in Figure 1.

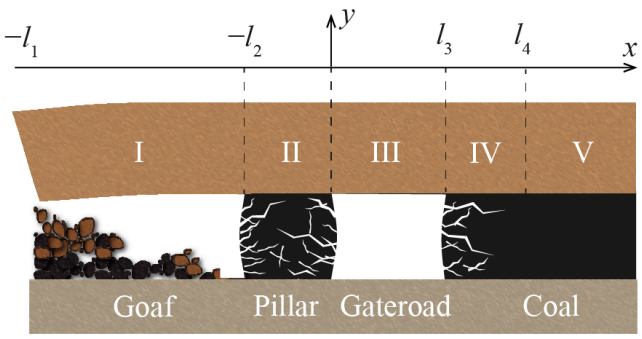


Figure 1. Mechanical structure of the coal pillar and hard roof.

According to different loads on the roof and the supporting conditions of the foundation, the mechanical models of rock beams I–V are shown in Figures 2–6.

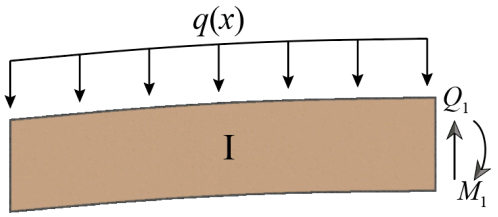


Figure 2. Mechanical model of rock beam I.

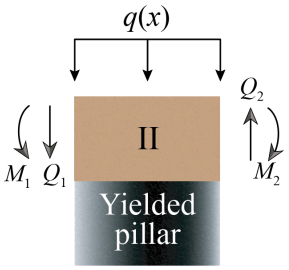


Figure 3. Mechanical model of rock beam II.

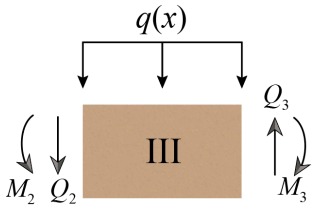


Figure 4. Mechanical model of rock beam III.

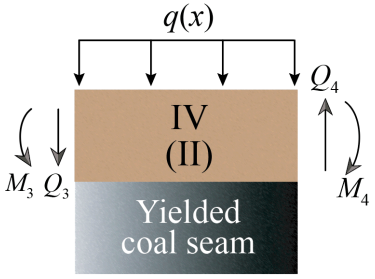


Figure 5. Mechanical model of rock beam IV.

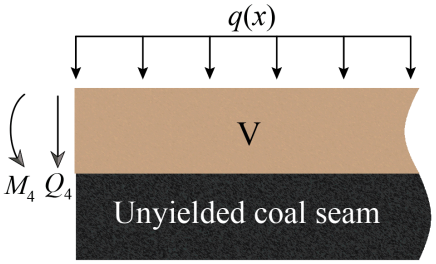


Figure 6. Mechanical model of rock beam V.

2.1. Mechanical Model of Rock Beam I

Rock beam I is a lateral suspended roof that has not been broken and spanned in the goaf of the adjacent working face. It can be regarded as a cantilever beam structure here; that is, the left end of rock beam I is the free end, and the right side is subjected to the bending moment M_1 and shear force Q_1 at the I–II interface of the rock beam. The upper part is loaded $q(x)$, and its mechanical model is shown in Figure 2.

According to the mechanics of materials, the deflection $y_{\mathrm{I}}(x)$, rotation angles $\theta_{\mathrm{I}}(x)$, bending moment $M_{\mathrm{I}}(x)$ and shear force $Q_{\mathrm{I}}(x)$ of rock beam I can be expressed as

$$\left.\begin{array}{l} y_{\mathrm{I}}(x) = -\int \theta_{\mathrm{I}}(x)dx + C_{\mathrm{I1}} \\ \theta_{\mathrm{I}}(x) = -\dfrac{\int M_{\mathrm{I}}(x)dx}{-EI} + C_{\mathrm{I2}} \\ M_{\mathrm{I}}(x) = M_1 + Q_1(x - l_{\mathrm{s}}) - \int_0^{x-l_2} q_{\mathrm{ic}}(l_2 + t)(x - l_2 - t)dt \\ Q_{\mathrm{I}}(x) = -\dfrac{dM_{\mathrm{I}}(x)}{dx} \end{array}\right\} (-l_1 \le x < -l_2) \quad (1)$$

In the equation, C_{I1} and C_{I2} are integral constants, E is the plane strain modulus of the rock beam, and I is the moment of inertia of the rock beam.

2.2. Mechanical Model of Rock Beam II

Rock beam II is located above the coal pillar. The left end of rock beam II is subjected to bending moment M_1 and shear force Q_2 at the rock beam I-II interface, the right end is subjected to bending moment M_2 and shear force Q_2 at the rock beam II-III interface, the upper part is subjected to load $q(x)$, and the lower part is subjected to the supporting reaction force provided by the plastic coal pillar. Its mechanical model is shown in Figure 3.

If rock beam II is regarded as a finite elastic foundation beam, the deflection $y_{\mathrm{II}}(x)$, rotation angle $\theta_{\mathrm{II}}(x)$, bending moment $M_{\mathrm{II}}(x)$ and shear force $Q_{\mathrm{II}}(x)$ of rock beam II can be expressed as

$$\left.\begin{aligned} y_{\mathrm{II}}(x) &= y_0F_1(\lambda x)+\frac{1}{\lambda}\theta_0F_2(\lambda x)-\frac{1}{\lambda^2}\frac{1}{EI}M_0F_3(\lambda x)\\ &\quad -\frac{1}{\lambda^3EI}Q_0F_4(\lambda x)+\frac{1}{\lambda^3EI}\int_0^x q_{\mathrm{ic}}(t)F_4[\lambda(x-t)]dt\\ \theta_{\mathrm{II}}(x) &= \frac{dy_{\mathrm{II}}(x)}{dx}\\ M_{\mathrm{II}}(x) &= -EI\frac{d\theta_{\mathrm{II}}(x)}{dx}\\ Q_{\mathrm{II}}(x) &= \frac{dM_{\mathrm{II}}(x)}{dx} \end{aligned}\right\}(-l_2<x\le 0) \tag{2}$$

In the formula, y_0, θ_0, M_0, and Q_0 represent the deflection, rotation angle, bending moment and shear force at the left boundary of the coal pillar on the rigid roof. $F_1(\lambda x)$–$F_4(\lambda x)$ are intermediate variables given to simplify the expression

$$\left.\begin{aligned} F_1(\lambda x) &= \cosh\lambda x\cos\lambda x\\ F_2(\lambda x) &= \tfrac{1}{2}(\cosh\lambda x\sin\lambda x+\sinh\lambda x\cos\lambda x)\\ F_3(\lambda x) &= \tfrac{1}{2}\sinh\lambda x\sin\lambda x\\ F_4(\lambda x) &= \tfrac{1}{4}(\cosh\lambda x\sin\lambda x-\sinh\lambda x\cos\lambda x) \end{aligned}\right\} \tag{3}$$

In the formula, $\lambda=\sqrt[4]{k_n(x_n)/4EI}$, $k_n(x_n)$ represent the stiffness of the coal seam. Rock beam II is divided into segments, and the mechanical expression of the plastic coal body is achieved by setting the corresponding equivalent plastic stiffness for each segment.

2.3. Mechanical Model of Rock Beam III

Rock beam III is located above the roadway. The left end of rock beam III is subjected to the bending moment M_2 and shear force Q_2 at the interface of rock beam II-III, and the right end is subjected to the bending moment M_3 and shear force Q_3 at the interface of rock beam III-IV. The upper part is loaded and the lower part is not supported by foundation. The mechanical model is shown in Figure 4.

According to material mechanics, the deflection $y_{\mathrm{III}}(x)$, rotation $\theta_{\mathrm{III}}(x)$, bending moment $M_{\mathrm{III}}(x)$ and shear force $Q_{\mathrm{III}}(x)$ of rock beam III can be expressed as follows:

$$\left.\begin{aligned} y_{\mathrm{III}}(x) &= -\int\theta_{\mathrm{III}}(x)dx+C_{\mathrm{III1}}\\ \theta_{\mathrm{III}}(x) &= -\frac{\int M_{\mathrm{III}}(x)dx}{-EI}+C_{\mathrm{III2}}\\ M_{\mathrm{III}}(x) &= M_2+Q_2x-\int_0^x q(t)(x-t)dt\\ Q_{\mathrm{III}}(x) &= -\frac{dM_{\mathrm{III}}(x)}{dx} \end{aligned}\right\}(0\le x<l_3) \tag{4}$$

In the formula, C_{III1} and C_{III2} are integral constants, E represents the plane strain modulus of the rock beam, and I denotes the moment of inertia of the rock beam.

2.4. Mechanical Model of Rock Beam IV

Rock beam IV is a finite-length beam supported by plastic coal in front of the working face. The left end of rock beam IV is subjected to bending moment M_3 and shear force Q_3 at the interface between rock beams III and IV, while the right end is subjected to bending moment M_4 and shear force Q_4 at the interface between rock beams IV and V. The upper part is subjected to a non-uniformly distributed load $q(x)$, and the lower part is subjected to the supporting reaction force provided by the plastic coal; its mechanical model is shown

in Figure 5. The mechanical model of beam IV is consistent with that of beam II, and is not described in detail here.

2.5. Mechanical Model of Rock Beam V

Rock beam V is a semi-infinite beam supported by the elastic coal body from the interior of the solid coal. The left end of rock beam V is subjected to bending moment M_4 and shear force Q_4 at the interface between rock beams IV and V. The upper part is subjected to a non-uniformly distributed load $q(x)$, while the lower part is subjected to the supporting reaction force provided by the elastic coal body. Its mechanical model is shown in Figure 6.

Considering rock beam V as a semi-infinite elastic foundation beam, the deflection $y_{\mathrm{V}}(x)$, rotation $\theta_{\mathrm{V}}(x)$, bending moment $M_{\mathrm{V}}(x)$, and shear force $Q_{\mathrm{V}}(x)$ of rock beam V can be expressed as follows:

$$\left.\begin{array}{l} y_{\mathrm{V}}(x) = y_{\mathrm{V_DL}}(x) + y_{\mathrm{V_BM}}(x) + y_{\mathrm{V_SF}}(x) \\ \theta_{\mathrm{V}}(x) = \frac{dy_{\mathrm{V}}(x)}{dx} \\ M_{\mathrm{V}}(x) = -EI\frac{d\theta_{\mathrm{V}}(x)}{dx} \\ Q_{\mathrm{V}}(x) = \frac{dM_{\mathrm{V}}(x)}{dx} \end{array}\right\} (l_4 \le x) \tag{5}$$

In the formula, $y_{\mathrm{V_BM}}(x)$ and $y_{\mathrm{V_BM}}(x)$ are the deflection of the beam caused by the distributed load $q(x)$, the end bending moment M_4 and the end shear force Q_4, respectively. The specific solution process is more complicated due to the calculation process, which has been discussed in detail in the relevant literature, and is not detailed here.

In terms of the strain energy density, it can be stored in hard roof strata through bending moments and shear stresses. Given that bending-induced strain energy constitutes the predominant component, it represents the primary focus of this investigation. The density is determined by the following equation:

$$\frac{dU}{dx} = \frac{1}{2}M(x)d\theta = \frac{M^2(x)dx}{2EI} \tag{6}$$

By utilizing the initial boundary conditions at the end face of the rock beam and the continuity conditions at the interface, and combining the mechanical equations of rock beam I and rock beam V, the mechanical model of the hard roof can be solved [16,17,27]. Using the constructed roof mechanical model, the stress state of the roof can be quantified, thereby enabling analytical analysis of the coal pillar size and its control effect on the roof.

3. Case Study

Coal mine A is located in Shaanxi Province, China. Within a range of 100 m from the roof of the 21,409 working face, there exists one or two continuously developed composite thick and hard sandstone layers. These layers have a uniaxial compressive strength ranging from 34.5 to 67.9 MPa, classifying them as medium- to high-strength sandstone. The thickness of these layers is between 13 and 38 m, typical of thick and hard sandstone formations, with a burial depth of 400–500 m. A 6 m small coal pillar is reserved to the west of the 21,409 working face haulage roadway, adjacent to the goaf of the 21,408 working face. The roof is composed of a sandstone layer with an average thickness of approximately 25 m.

Based on the mechanical parameters of coal and rock strata in the 21,409 working face of coal mine A, this section will use the above mechanical model of working face tendency to analyze the mechanical state of the hard roof in the 21,409 working face through specific numerical examples, focusing on the distribution of tensile shear stress, elastic strain energy

and advance abutment pressure along the hard roof. The specific parameters are shown in Table 1.

Table 1. Parameters for calculating the mechanical state of the hard roof.

Model Parameter	Numerical Value
Coal pillar width l_{mz}	6, 10, 20 m
Roof elastic modulus E	14.8 GPa
Thickness of roof h	25 m
Suspended roof distance in tendency direction l_{xd}	25 m
Width of return airway l_{hf}	5 m
Elastic modulus of coal seam E	3.95 GPa
Overburden load q	10 MPa

In this study, narrow pillars are classified as those with a width of ≤6 m, intermediate-width pillars as 6 m < width < 20 m, and wide pillars as ≥20 m. Using the mechanical model of the coal pillar–hard roof established in Section 2, the roof deflection, bending moment, shear force and elastic strain energy density of the 21,409 working face are obtained according to the parameters of the above table, as shown in Figure 7.

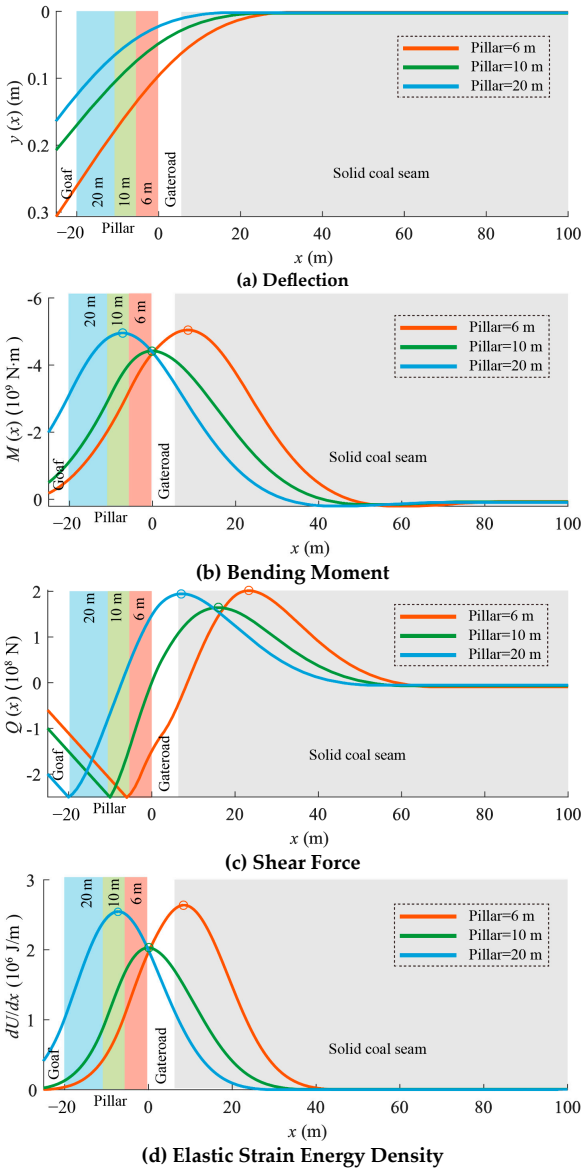


Figure 7. Mechanical state of the hard roof under different coal pillar widths.

Figure 7 reveals the deformation and stress characteristics of the roof under different coal pillar widths. In order to facilitate the comparison of the calculation results under different coal pillar widths, the boundary between the roadway and the coal pillar is set to x = 0.

Figure 7a is the calculation result of the deflection of the hard roof, which shows that the deflection of the roof begins to sink from about x = 20 to 30 m inside the solid coal on the right side of the roadway, and reaches the maximum in the goaf on the left side of the coal pillar. As the width of the coal pillar increases from 6 m to 20 m, the overall deflection of the roof is significantly controlled. In particular, the decrease in deflection near the roadway means that the deformation of the roadway is reduced, which has a positive effect on the roadway support for the deformation control of the surrounding rock.

Figure 7b is the calculation result of the bending moment of the hard roof. The bending moment indicates the tensile stress state of the roof plate. It can be observed that with an increase in the width of the coal pillar, the peak position and peak value of the bending moment change significantly. When the width of the coal pillar is 6 m, the peak bending moment is located above the solid coal on the right side of the roadway. When the width of the coal pillar is 10 m, the peak bending moment is located above the interface between the roadway and the coal pillar. When the width of the coal pillar increases to 20 m, the peak bending moment is transferred to the top of the coal pillar. The peak bending moment controls the fracture position of the roof, so the above results show that as the width of the coal pillar increases, the laterally selected roof fracture point will be transferred from the top of the solid coal to the top of the coal pillar. When the roof breaking point is located above the coal pillar, additional disturbance will be applied to the coal pillar, and the load of the coal pillar will increase significantly, which will significantly increase the risk of impact instability of the coal pillar for the rock burst mine.

Figure 7c is the calculation result of the shear force of the hard roof, and the spatial position that controls the shear fracture of the roof is established. Analysis of the data in the figure reveals that there are two typical distribution areas for the shear stress extremum: one is located at the left boundary of the coal pillar, and the other is distributed in the solid coal area on the right side of the roadway. With an increase in coal pillar width, the extreme value of shear stress on the solid coal side shows the law of migration from the deep part of the coal body to the direction of the roadway. The specific performance is as follows: when the width of the coal pillar is 6 m, the peak shear stress appears at about 25 m inside the coal body; when the width of the coal pillar increases to 20 m, the peak position migrates to about 1 m inside the solid coal on the right side of the roadway. This phenomenon reveals that an increase in coal pillar width causes the roof shear fracture position to gradually approach the near-field area of the roadway. After the shear fracture of the roof, the load will be significantly concentrated on the left coal pillar of the roadway and the near-field surrounding rock around the roadway. For rock burst mines, this change in load distribution characteristics will significantly increase the risk of rock burst instability in coal pillars and surrounding rocks of near-field roadways.

Figure 7d shows the calculation results of the elastic strain energy density of the hard roof. Due to the functional relationship between the elastic strain energy density and the bending moment, the spatial distribution trend is consistent with the bending moment calculation results, but there are differences in the physical meaning between the two: the elastic strain energy density characterizes the characteristics of the elastic strain energy stored in the hard roof, and the energy will be converted into the dynamic impact energy at the moment of the roof breaking to propagate around the coal body. The analysis shows that with an increase in coal pillar width, the maximum elastic strain energy accumulation area of the roof presents the evolution law of the transfer from the solid coal on the right

side of the roadway to the left coal pillar. When the elastic strain energy is released in the coal pillar area, it will have a significant impact load effect on the coal pillar. For rock burst mines, if the load position is close to the near-field area of the roadway, the risk of impact instability of the coal pillar will be significantly increased.

The above results reveal the complex influence of the increase in coal pillar width on the rock burst mine by calculating and analyzing the deflection, bending moment, shear force and elastic strain energy density of the hard roof. As the width of the coal pillar increases from 6 m to 20 m, although the deflection of the roof near the roadway is significantly reduced, which is conducive to roadway support and surrounding rock deformation control, it also brings a higher risk of impact instability. From the perspective of mechanical response, the peak position of bending moment increases with the width of coal pillar, which is gradually transferred from the upper part of solid coal on the right side of the roadway to the upper part of the coal pillar, resulting in a change in the tensile fracture position of the roof and an increase in additional disturbance and load of the coal pillar. The extreme value distribution of shear stress shows that the peak position of the solid coal side migrates to the near-field of the roadway, prompting the roof shear fracture position to approach the roadway, resulting in the load concentration on the left coal pillar of the roadway and surrounding rock in the near-field after fracture. In addition, the roof elastic strain energy gathering area is also transferred from the solid coal to the coal pillar, and the dynamic impact energy released during the fracture directly acts on the coal pillar. The comprehensive effect of the above mechanical response makes the load and disturbance of the coal pillar increase significantly. In the rock burst mine, the risk of rock burst instability of the coal pillar and the surrounding rock of the near-field roadway is greatly improved.

Based on the analytical model, this section systematically analyzes the evolution law of the mechanical characteristics of hard roofs under different coal pillar width conditions. However, there are limitations in only studying the hard roof, and the distribution characteristics of coal seam abutment pressure and the movement law of overlying strata in the stope still need to be discussed in depth. Therefore, in the next section, numerical simulation methods will be employed to systematically study the evolution laws of mechanical responses in the stope–coal body system under different coal pillar widths. The comprehensive influence mechanism of coal pillar width on the movement of overlying strata, distribution of abutment pressure, and mechanical state of coal will be analyzed and revealed, providing a more comprehensive theoretical basis for the rational setting of coal pillars in rock burst mines.

4. PFC-FLAC Coupled Simulation

The continuum simulation method, although widely applied in fields such as underground engineering and capable of effectively simulating the stress distribution in mining areas, cannot depict discontinuous failure behaviors such as roof fractures. The Discrete Element Method can simulate material crack evolution and damage quantification from a mesoscale perspective, but it is limited by particle contact calculations and has difficulty directly obtaining the macroscopic stress field. Given the complementarity of the two in continuous–discontinuous medium simulation, this project adopts the PFC-FLAC coupling method. Through PFC, the process of overburden strata fracturing and caving is visually reproduced. FLAC is utilized to impose stress boundary conditions and analyze the stress distribution pattern in the stope. The surrounding boundaries and coal seams of the constructed numerical model will be simulated using the FLAC model, while the remaining parts will be simulated using the PFC model. There are two commonly used PFC-FLAC

coupling methods, namely Ball–Zone coupling and Wall–Zone coupling, and the latter is adopted here.

4.1. Calibration of PFC Contact Parameters

The calibration of mesoscale parameters for discrete element materials is one of the most fundamental and crucial issues in the field of discrete element research [28,29]. Through scientific calibration of mesoscale parameters for discrete element materials, the macroscopic mechanical parameters of materials can be aligned with the mechanical test parameters in the laboratory, which is a necessary condition for accurate simulation research. Ji and Karlovšek [28,30] used a differential evolution global optimization algorithm to calibrate the material deformation and strength mechanical parameters to 1% relative error in PFC2D. Compared with other calibration methods, the global optimization algorithm shows excellent robustness and accuracy. Given that existing research has demonstrated the excellent performance of the differential evolution algorithm in the application of mesoscale parameter calibration for discrete element materials, this study also adopts this method to carry out mesoscale parameter calibration for PFC materials. It is specifically agreed that in the following text, the subscript "mi" represents the PFC contact parameters (microparameters) of PFC materials, while the subscript "ma" represents the experimental mechanical parameters (macroparameters) of the materials. The main issues involved in the calibration process include PFC mechanical testing, construction of the objective function, and determination of the range of PFC contact parameters.

4.1.1. PFC Mechanical Test

Similar to the measurement of rock mechanical parameters under laboratory conditions, corresponding mechanical experiments need to be carried out in PFC to determine the mechanical parameters of materials. For example, the uniaxial compressive strength, elastic modulus and Poisson's ratio of the specimen are measured by PFC uniaxial compression tests, and the uniaxial tensile strength of the specimen is measured by direct tensile tests. It should be noted that it is difficult to carry out direct tensile tests under laboratory conditions, so the Brazilian splitting test is often used to determine the tensile strength of specimens. Compared with the Brazilian splitting test, the tensile strength measured by the direct tensile test is more accurate. Therefore, the former is preferred in PFC to measure the tensile strength of specimens.

Each set of mechanical tests in PFC includes three main steps: generating PFC rock specimens, conducting uniaxial compression tests, and conducting direct tensile tests. In uniaxial compression and direct tensile tests, the test loading rate is controlled by the strain rate $\dot{\varepsilon}_{c/t}$, $\dot{\varepsilon}$(with the subscript "c" denoting uniaxial compression tests and the subscript "t" denoting direct tensile tests).

$$\dot{\varepsilon}_{\mathrm{c/t}} = \frac{|v_{\mathrm{c/t}}|}{0.5 \times H} \tag{7}$$

In the formula, v_{c} represents the relative movement speed of the upper and lower loading walls in the uniaxial compression test, v_{t} denotes the opposite movement speed of the upper and lower loading particles in the direct tensile test, and H stands for the height of the specimen.

In the uniaxial compression test, compression loading is simulated by setting up walls that move towards each other at the top and bottom of the model. In the direct tensile test, tensile loading is simulated by controlling the particles at the top and bottom edges of the specimen to move in opposite directions within a certain range. The geometric shape of the specimen is defined by its height H and width W. The geometric shape of the specimen is defined by its height H and width W, with an aspect ratio H/W = 1, and about 25 particles are distributed along its width, as shown in Figure 8.

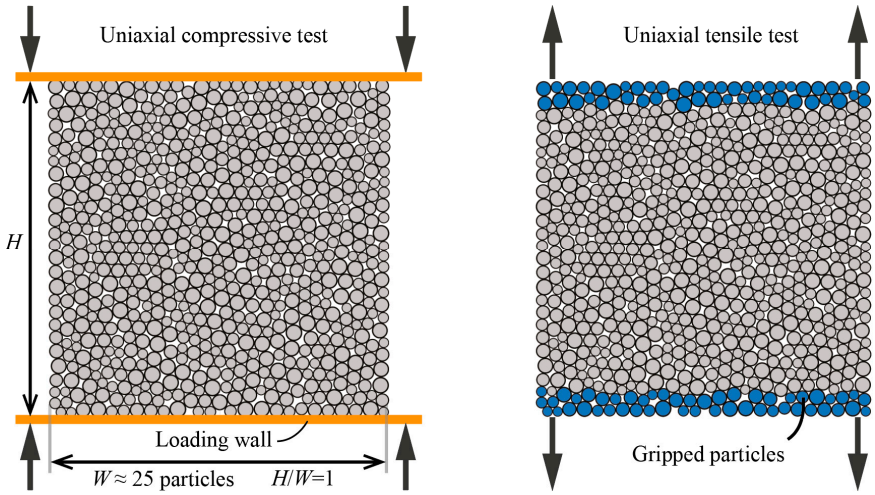


Figure 8. Mechanical tests for calibrating PFC contact parameters [30].

The total number of particles in the constructed test specimen is approximately 700, ensuring that neither significant errors due to an insufficient number of particles nor increased computation times due to an excessive number of particles occur. In terms of material gradation, the ratio of the maximum radius of the particle to the minimum radius $r_{\max}/r_{\min}$ = 1.66, and the initial configuration gap of the contact model should usually be less than the minimum particle radius, which is set to 0.4 $r_{\min}$.

4.1.2. Construction of Objective Function

Calibrating PFC contact parameters using optimization algorithms is essentially a process of continuously trying different PFC contact parameter values and gradually approximating the target macroscopic mechanical parameters. Therefore, it is necessary to construct an objective function to quantify the relative error between the current simulated material's macroscopic mechanical parameters and the target values. The tested PFC contact parameters are the input variables, while the macroscopic mechanical parameters of the specimen are the output variables. Then the calibration is to solve the optimization problem of the minimum value of the above objective function $f(p_{\mathrm{mi}})$.

$$f(p_{\mathrm{mi}}) = RE_{\mathrm{sum}} = \sum RE(p_{\mathrm{ma_sim}}, p_{\mathrm{ma_tar}}) \tag{8}$$

In the formula, RE_{sum} represents the sum of relative errors of various macroscopic mechanical parameters. $p_{\mathrm{ma_sim}} = \mathrm{PFC}(p_{\mathrm{mi}})$ denotes the simulated measured macroscopic mechanical parameters of the material, which are obtained through PFC mechanical testing based on the given PFC contact parameters. $p_{\mathrm{ma_tar}}$ signifies the target macroscopic mechanical parameter.

In the simulation analysis of rock-like materials, if the elastic mechanical behavior of the material is mainly concerned, the focus of the calibration is the elastic modulus and Poisson's ratio of the material. By introducing the weight factor (w_i) of macroscopic mechanical parameters, the priority of different macroscopic mechanical parameters is set in the calibration process.

$$RE_{\mathrm{sum}} = f(p_{\mathrm{mi}}) = \sum (w_i \cdot RE(\mathrm{PFC}(p_{i,\,\mathrm{mi}}), p_{i,\mathrm{ma_tar}})) \ (\sum w_i = 1) \tag{9}$$

In this report, both material deformation and strength need to be considered; the uniaxial compressive strength, uniaxial tensile strength, elastic modulus, and Poisson's ratio are considered as the parameters requiring calibration. Each parameter is assigned an equal weight factor of 0.25. Regarding calibration accuracy, relevant research has achieved

a weighted relative error below 1% between the calibrated macroscopic mechanical parameters and the target values. This report adopts the same calibration accuracy standard, $RE_{\text{sum}} = 0.01$, as the convergence criterion for the optimization algorithm. For Mohr–Coulomb parameter calibration, the internal friction angle and cohesion can be analytically derived from the uniaxial compressive strength and uniaxial tensile strength; therefore, they are not listed as mechanical parameters requiring direct calibration.

4.1.3. PFC Contact Parameters

When calibrating PFC contact parameters using optimization algorithms, it is necessary to search for optimal parameter values within predefined ranges. Establishing a reasonable range for PFC contact parameters must satisfy two fundamental principles: the range must encompass the optimal value to ensure the algorithm can find it, and it should be as narrow as possible to expedite the search process. To maximize calibration success probability, a relatively large parameter range is adopted here. The range is defined by the parameter center value (p_{cen}) and a boundary offset (p_{bia}). Thus, the lower bound is $p_{\text{low}} = p_{\text{cen}} \times (1 - p_{\text{bia}})$, and the upper bound is $p_{low} = p_{\text{cen}} \times (1 - p_{\text{bia}})$. The PFC contact parameter search ranges are illustrated in Table 2.

Table 2. PFC contact parameters (flat-joint model) with calibration ranges.

PFC Contact Parameter (p_{mi})	Center Value (p_{cen})	Boundary Offset (p_{bia})
Cohesion	Target cohesion	0.9
Tensile strength	Target tensile strength	0.9
Effective modulus	Target Young's modulus	0.9
Normal stiffness	3.0	0.9
Friction coefficient	0.5	0.9
Friction angle	40°	0.9

4.1.4. Calibration Results

For simplification, three material types will be used in the numerical simulation: coal, hard roof sandstone, and the immediate roof layer mudstone. The mechanical parameters of these coal–rock masses are shown in Table 3.

Table 3. Mechanical parameters of coal and rock masses for simulations.

Lithology	Density (kg/m^3)	UCS (MPa)	UTS (MPa)	Young's Modulus (GPa)	Poisson's Ratio	Cohesion (MPa)	Friction Angle (°)	Simulation Method
Mudstone	2520	30.79	1.38	1.35	0.22	3.26	66.09	PFC + FLAC
Sandstone	2557	55.63	4.70	14.80	0.32	8.08	57.59	PFC + FLAC
Coal	1540	25.62	1.15	3.95	0.34	2.71	66.08	FLAC

Using the macroscopic mechanical parameters from Table 3 as calibration targets, the global optimization algorithm described above was employed for parameter calibration, with a convergence criterion of 1% relative error ($RE_{sum} = 0.01$).

The stress–strain curves from the uniaxial compression and direct tensile tests for the two calibrated rock types are shown in Figure 9. The elastic modulus and Poisson's ratio were calculated using the stress and corresponding strain at 50% of the peak stress, where the rock mass is still predominantly in the linear elastic deformation stage.

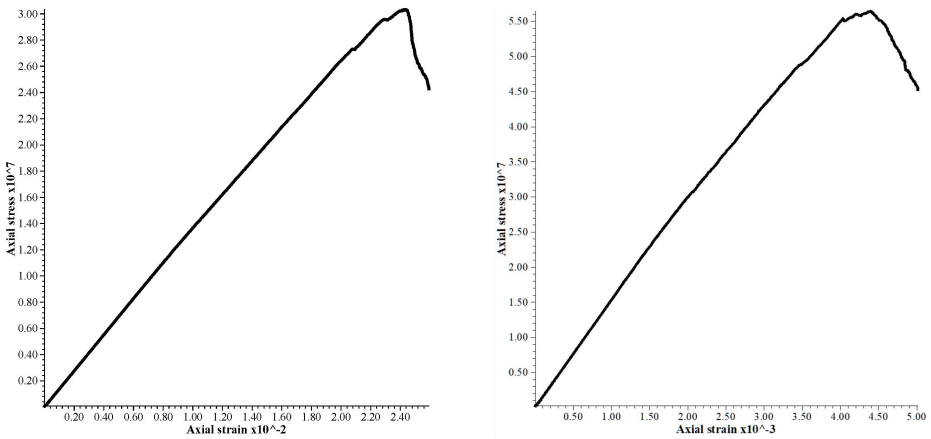


Figure 9. Stress–strain curves from PFC uniaxial compression tests.

The calibrated PFC contact parameters corresponding to the macroscopic parameters in Table 3 are presented in Table 4. Other PFC contact parameter settings include porosity = 10%, minimum particle radius = 0.3 m, maximum-to-minimum particle radius ratio = 1.66, number of contact elements = 4, and initial surface gap = 0.12 m.

Table 4. Calibrated PFC contact parameters for rock specimens (flat-joint model).

Lithology	Effective Modulus (GPa)	Stiffness Ratio	Friction Coefficient	Tensile Strength (MPa)	Cohesion (MPa)	Friction Angle (°)
Mudstone	1.17	1.74	0.55	1.70	1.01	47.82
Sandstone	14.25	2.71	0.58	5.78	22.92	18.29

It is important to note that the PFC contact parameters shown in Table 4 present one set of optimal values for the corresponding macroscopic parameters. PFC contact parameter calibration is closely tied to the discrete element material generation method. This report references the PFC example "Rock testing" for material generation; therefore, the obtained parameter values may not be directly applicable to other discrete element generation methods. Technical details regarding the calibration of PFC contact parameters and the sensitivity analysis have been extensively reported by Ji and Karlovšek [28] and will not be discussed in this study.

Following the calibration of PFC contact parameters, numerical simulation will be conducted using the 21,409 longwall panel as the background scenario to investigate the characteristics of overburden movement and surrounding rock stress distribution under different coal pillar widths. The simulation process includes geometric model construction, application of boundary conditions and initialization, setup of monitoring schemes, and excavation sequences.

4.2. Model Design

To fully simulate the influence of the adjacent working face goaf, the model dimensions are 400 m in the horizontal direction and 85 m in the vertical direction. The model stratigraphy consists of floor thickness = 10 m, coal seam thickness = 5 m, immediate roof = hard sandstone (25 m thick), and an overlying immediate roof layer of mudstone (3 m thick), as shown. Based on in situ stress measurements, a vertical stress of 9 MPa is applied to the model top. The lateral pressure coefficient is set to 1.5. Normal displacement constraints are applied to the left, right, and bottom boundaries. The adjacent goaf width is set to 200 m. The roadway width is 5 m. The section coal pillar lies between the roadway

and the goaf. The solid coal of the current working face is located to the right of the roadway (as shown in Figure 10).

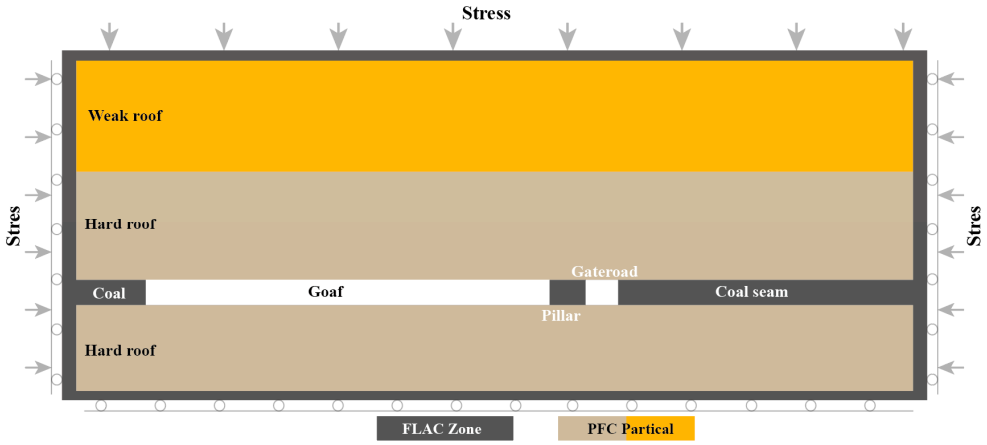


Figure 10. Schematic of the PFC-FLAC coupled numerical model.

Specific control parameters are listed in Table 5.

Table 5. Coal pillar width settings for abutment pressure analysis.

Control Factor	Initial Value	Test Values
Coal Pillar Width (m)	6	10, 20, 30, 40

After applying the boundary conditions, the model undergoes initialization calculations. Under the applied top stress, the model experiences initial settlement. The vertical settlement is shown in Figure 11. By setting consistent scales for the PFC particle settlement and FLAC mesh settlement contours, it can be observed that the particle settlement in PFC is uniform and smooth, aligning well with the settlement trend of the FLAC mesh. This indicates good consistency in the mechanical properties of the calibrated PFC materials and their FLAC counterparts. After calculating convergence, the particle and mesh displacements are reset to zero, completing model initialization.

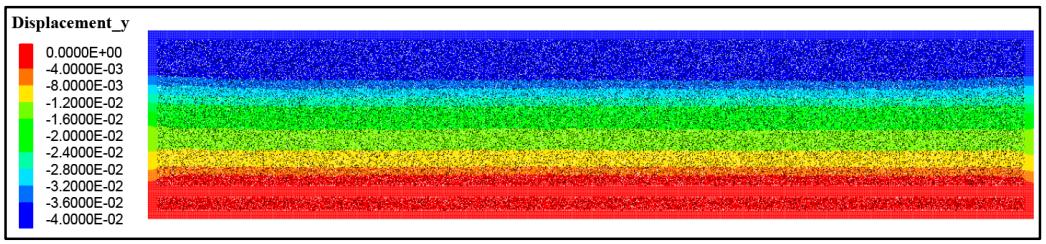


Figure 11. Initial vertical settlement of the model under in situ stress.

5. Results and Discussion

Following initial in situ stress equilibrium, model excavation is performed in two stages. Stage 1 involves excavating the adjacent working face to replicate the lateral goaf stress environment. Stage 2 involves roadway excavation after reserving a pillar of the specified width, with calculation proceeding until model convergence. The analysis focuses on the stress and deformation characteristics of the coal pillar, roadway, and near-field solid coal, specifically investigating the distribution and evolution of abutment pressure above the pillar and lateral abutment pressure within the coal mass.

5.1. Strata Movement

Vertical displacement effectively characterizes the deformation of the pillar and roadway surrounding rock. Given that the goaf roof has fully caved, the maximum displacement in the stope occurs within the adjacent goaf to the left of the pillar. To highlight the vertical deformation characteristics of the roadway surrounding rock and the influence of the adjacent lateral goaf on the current working face, the upper limit of the vertical displacement contour display is set to 0.05 m. This accentuates the deformation features of the pillar and roadway surrounding rock under different pillar widths (as shown in Figure 12).

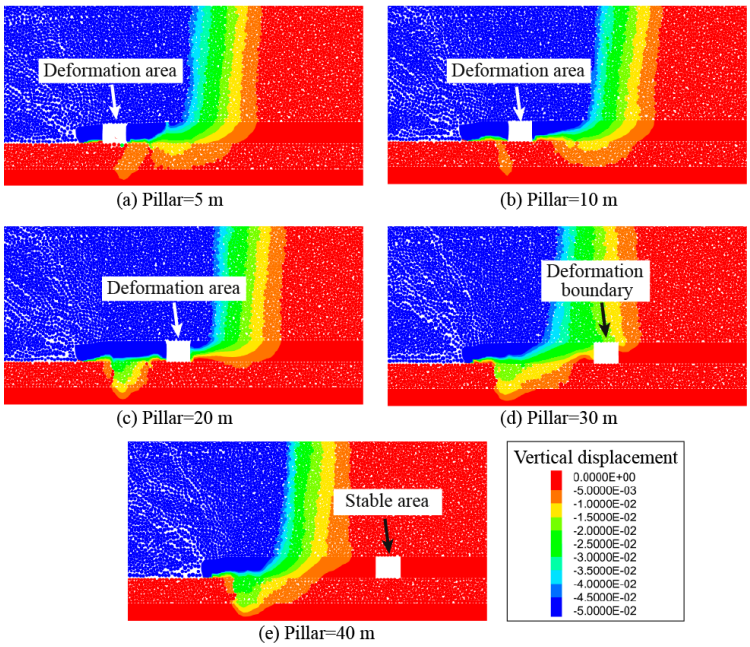


Figure 12. Vertical displacement of overlying strata under different coal pillar widths.

Figure 12 shows that under all pillar widths, the immediate roof of the adjacent working face has fully caved without forming a hanging roof. The vertical deformation of the surrounding rock exhibits distinct zoning. The blue-to-red transition zone corresponds to the stable area and the deformation gradient area, reflecting the influence range of the adjacent goaf. Comparing the five pillar width scenarios reveals that the influence range of the adjacent goaf on the current working face is consistently around 30 m. Deformation intensity increases significantly closer to the goaf. For example, at a pillar width of 5 m, the compressive deformation on the pillar's left side is markedly higher than on the right side. Concurrently, due to the high overall deformation of the pillar, the solid coal on the roadway's right side also exhibits considerable deformation. At a pillar width of 10 m, significant compressive deformation persists on the pillar's left side, but deformation on both sides of the roadway is notably reduced. When the pillar width exceeds 30 m, the correlation between goaf deformation and pillar/roadway deformation weakens. Roadway surrounding rock deformation becomes uniform and low in magnitude, indicating the roadway is largely isolated from the lateral load influence of the goaf. This signifies that the pillar has become the primary load-bearing element for the lateral abutment pressure.

5.2. Stress Redistribution

To quantify stress transfer within the stope and the load-bearing characteristics of the pillar, the evolution of force chains in the PFC model region and vertical stress in the FLAC model region under different pillar widths is further analyzed (as shown in Figure 13).

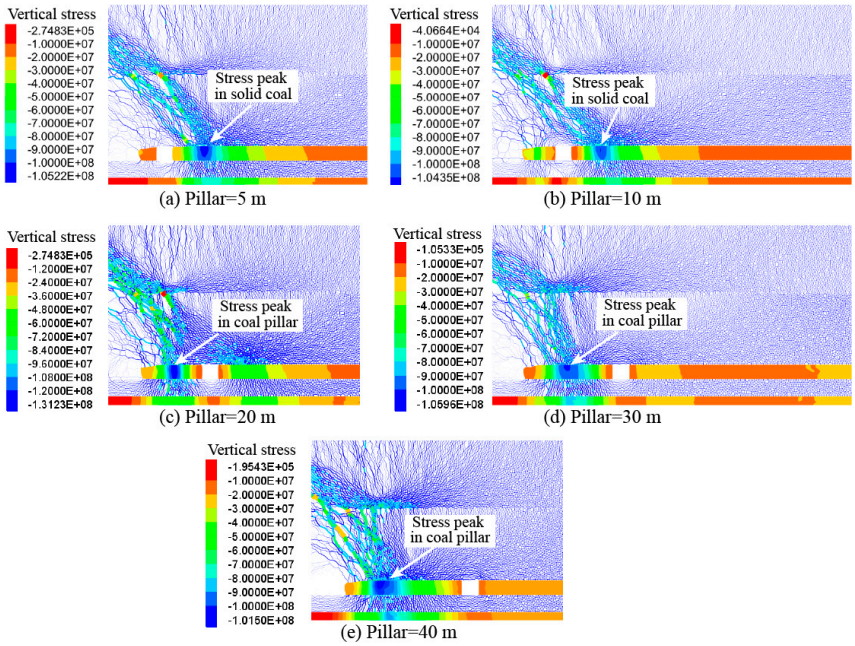


Figure 13. Force chains and vertical stress of overlying strata under different coal pillar widths.

Figure 13 clearly illustrates the evolution of stress concentration zones within the coal mass. Bending subsidence of the lateral goaf causes the overburden to transfer stress via force chains to the solid coal of the current working face. The contact points between force chains in the PFC region and the coal seam correspond to the peak lateral pressure zones within the coal. At a pillar width of 5 m, significant pillar deformation causes the lateral stress transfer force chains to bypass the pillar and concentrate within the solid coal on the roadway's right side. No stress concentration occurs within the pillar itself; the entire pillar is in a low-stress state. Nevertheless, the section pillar still provides some support to the goaf-side roadway; despite exhibiting large deformation, the roadway remains overall stable. At a pillar width of 10 m, force chains related to lateral stress transfer show some increase above the pillar but remain primarily concentrated in the solid coal on the roadway's right side. At a pillar width of 20 m, significant stress concentration within the near-field roadway surrounding rock disappears. Lateral stress transfer force chains concentrate mainly within the pillar itself, indicating that the section pillar exhibits more pronounced stress concentration compared to the solid coal side. This stress concentration is located only 5–10 m from the roadway. Combined with roof fracturing and mining disturbance, this scenario is prone to inducing coal bursts. As pillar width increases further, the concentration point of the lateral stress transfer force chains remains relatively stable, consistently located approximately 12–14 m from the pillar's left boundary. Regarding the peak lateral abutment pressure within the coal seam, it reaches its maximum value of about 131 MPa at a pillar width of 20 m. Under other pillar widths, the peak lateral abutment pressure remains relatively stable, ranging between 100 and 106 MPa.

To further quantify stress distribution within the pillar and coal seam, a vertical stress monitoring line was placed along the centerline of the coal seam FLAC model. The monitoring results are shown in Figure 14.

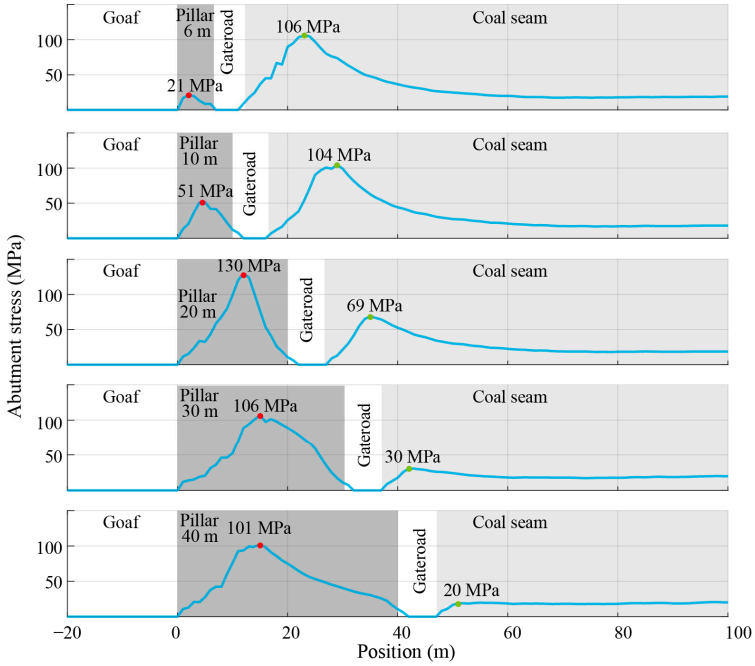


Figure 14. Lateral abutment stress distribution under different coal pillar widths.

Figure 14 indicates that changes in pillar width significantly affect the vertical stress in both the solid coal rib of the goaf-side roadway ahead of the working face and the section coal pillar. In terms of stress distribution profile shape, at a pillar width of 6 m, the peak abutment pressure above the pillar is about 21 MPa, essentially equal to the in situ stress of 20 MPa. The peak abutment pressure on the solid coal side is 106 MPa. This demonstrates that a 6 m pillar cannot effectively bear the lateral abutment pressure; consequently, the pressure transfers deeper into the coal mass. The pillar undergoes substantial plastic failure, preventing significant accumulation of elastic strain energy, which is beneficial for coal burst prevention. When the pillar width is sufficiently large ($\geq$20 m), the lateral abutment pressure on the section pillar increases rapidly from 51 MPa (at 10 m width) to 130 MPa. Increasing the width further to 30 m causes the lateral abutment pressure to peak and then decrease to 106 MPa. Subsequently, the peak pressure slowly decreases to around 101 MPa with further width increases. This reveals that section pillars wider than 6 m consistently exhibit a stress concentration exceeding in situ stress above them. For pillar widths between 10 and 20 m, the resulting peak abutment pressure occurs close to the roadway (<15 m) and is high in magnitude (>100 MPa). This condition is highly susceptible to inducing severe strata pressure dynamic manifestations. When pillar width increases beyond this range, the peak abutment pressure stabilizes relative to the adjacent goaf position, gradually moving farther away from the goaf-side roadway of the current working face, which is advantageous for coal burst prevention.

The above analysis demonstrates that both narrow pillars and wide pillars can positively contribute to coal burst prevention. Pillars between 10 m and 20 m, however, generate high lateral abutment pressures with peak values located dangerously close to the goaf-side roadway, making them unfavorable for coal burst prevention.

5.3. Research Limitations

This study employed both analytical and numerical methods to examine the mechanical behavior of coal pillars and surrounding roof strata. However, the analytical and numerical frameworks focus exclusively on static mechanical responses, omitting time-dependent deformation mechanisms such as coal pillar creep, stress relaxation, and

long-term strength degradation under sustained loading. Furthermore, the lack of field monitoring data, such as stress measurements within coal pillars and the solid coal mass, or roadway convergence records, limits empirical verification of the analytical and simulated results. Moreover, the proposed analytical model does not account for dynamic stress perturbations induced by mining-induced seismicity or roof fracturing events, which are key triggers for instability in burst-prone environments. Finally, the geological generalizability is constrained by focusing on a single case study configuration, without examining scenarios featuring thin/soft roofs, steeply inclined seams, or multi-seam interactions with residual pillars.

To address these limitations, subsequent investigations should prioritize collecting integrated field monitoring data, investigating long-term behavior, and developing dynamic modeling methods. Deployment of distributed fiber-optic sensing and stress sensors within coal pillars would enable real-time validation of stress redistribution patterns while capturing dynamic responses to roof fracturing. Concurrently, the PFC-FLAC modeling should be enhanced through the implementation of viscoplastic constitutive laws to simulate time-dependent pillar deformation and coupled dynamic modules to quantify stress wave propagation during seismic events. Case studies should expand geological scope by systematically varying key properties of roof strata, such as uniaxial compressive strength, thickness, and coal seam burial depth. Such efforts would establish width adjustment coefficients for different geological settings. Additionally, research should evaluate how support systems interact with time-dependent pillar behavior to develop integrated ground control strategies.

6. Conclusions

This study has systematically investigated the critical relationship between coal pillar width and geomechanical stability in burst-prone mines with thick, hard roof strata. Through integrated analytical modeling and coupled numerical simulations of a longwall panel case, the following conclusions are drawn:

(1) Pillar width dictates roof failure mechanics and stress redistribution. In the proposed case study, increasing pillar width from narrow to intermediate ranges (10–20 m) systematically shifts the locus of roof tensile fractures from solid coal toward the pillar center and migrates failure zones toward the roadway. Concurrently, elastic strain energy accumulation relocates from solid coal to the pillar area. This mechanistic shift concentrates loads directly onto pillars upon roof fracture, escalating instability risks.

(2) Intermediate pillar widths create a risk instability zone. Pillars between 10 and 20 m exhibit the most hazardous mechanical response. The lateral abutment pressures exceeding 130 MPa, positioned perilously close to the roadway. This combines with substantial elastic energy storage capacity and direct exposure to roof fracture dynamics, creating conditions highly conducive to coal burst. This width range should be deliberately avoided in burst-prone environments with hard roofs.

(3) Narrow and wide pillars offer distinct stability advantages. Pillars of 6 m or less undergo significant plastic deformation and exhibit low stress concentration, transferring loads deeper into the coal seam. Their limited capacity for elastic energy storage inherently reduces burst potential despite requiring robust asymmetric roadway support. Conversely, pillars wider than 40 m effectively isolate the roadway from goaf influences, stabilizing stress concentrations at lower magnitudes further from the roadway, thereby mitigating near-field dynamic risks.

(4) Effective ground control demands integrated pillar–roof–support design. Pillar width optimization is inseparable from roof behavior and tailored support strategies. The presence of thick, hard roofs imposes high, often asymmetric loads on pillars. Sup-

port systems must adapt to the specific stress environment induced by the chosen pillar width, emphasizing asymmetric reinforcement for narrow pillars. Continuous monitoring is essential to track stress evolution and time-dependent degradation.

(5) The validated methodology provides a practical design framework. The synergistic approach combining an analytical roof–pillar interaction model with rigorously calibrated simulations successfully captured the complex interplay of roof mechanics, pillar stress evolution, and failure modes. This framework offers a scientifically grounded basis for determining rational pillar widths that balance resource recovery, roadway stability, and coal burst mitigation under challenging hard roof conditions. Strategic selection toward either narrow or wide pillars emerges as the key safety principle.

This research establishes that pillar width is a primary control mechanism of the stability mechanics of coal mines operating under thick, hard roofs. Deliberate avoidance of the hazardous intermediate-width range coupled with an integrated design focused on the specific advantages of narrow or wide pillars provides a clear pathway toward safer and more efficient underground longwall mining.

Author Contributions: Conceptualization, S.J.; Methodology, J.K.; Validation, J.Z.; Formal analysis, C.L.; Investigation, Z.F.; Resources, Q.J. All authors have read and agreed to the published version of the manuscript.

Funding: This research was funded by the China Postdoctoral Science Foundation (Grant No. BX20240287; 2024MD764013; 2024MD753977; 2024MD753981), the National Natural Science Foundation of China (Grant No. 42402186; 52404098; 52404242), the Shaanxi Province Youth Talent Support Program Project (Grant No. 20250706), the Shaanxi Provincial Science Foundation (Grant No. 2024JC-YBMS-365), the State Key Laboratory Cultivation Base for Gas Geology and Gas Control (Henan Polytechnic University), and the State and Local Joint Engineering Laboratory for Gas Drainage & Ground Control of Deep Mines (Henan Polytechnic University).

Data Availability Statement: The original contributions presented in this study are included in the article. Further inquiries can be directed to the corresponding author.

Conflicts of Interest: The authors declare no conflict of interest.

List of Abbreviations

Abbreviations	Definition
PFC	Particle Flow Code
FLAC	Fast Lagrangian Analysis of Continua
DEM	Discrete Element Method
FEM	Finite Element Method

References

1. Zhu, Z.; Yao, Z.; Chen, K.; Lü, F.; Han, J.; Wang, L. Experimental study on the influence of width-height ratio on coal pillar type rock burst. *J. China Coal Soc.* **2024**, *49*, 1303–1317.
2. Van der Merwe, J.N. Coal pillar strength analysis based on size at the time of failure. *J. S. Afr. Inst. Min. Metall.* **2019**, *119*, 681–692. [CrossRef]
3. Zang, C.; Jiang, B.; Wang, X.; Wang, H.; Zhou, J.; Chen, M.; Cong, Y. Study on damage law and width optimization design of coal pillar with the discrete element method. *Geomech. Eng.* **2024**, *37*, 555–563.
4. Kumar, R.; Mandal, P.K.; Ghosh, N.; Das, A.J.; Banerjee, G. Design of Stable Parallelepiped Coal Pillars Considering Geotechnical Uncertainties. *Rock Mech. Rock Eng.* **2023**, *56*, 6581–6602. [CrossRef]
5. Najafi, M.; Jalali, S.E.; Bafghi, A.R.Y.; Sereshki, F. Prediction of the confidence interval for stability analysis of chain pillars in coal mines. *Saf. Sci.* **2011**, *49*, 651–657. [CrossRef]

6. Xu, X.; Wei, H.; Tian, S.; Zhang, B. Study on influence law of coal pillar size on roof break structure and fracture development in fully mechanized working face. *J. China Coal Soc.* **2015**, *40*, 850–855.
7. Xie, S.; Guo, F.; Wu, Y. Control Techniques for Gob-Side Entry Driving in an Extra-Thick Coal Seam with the Influence of Upper Residual Coal Pillar: A Case Study. *Energies* **2022**, *15*, 3620. [CrossRef]
8. Li, Q.; Li, J.; Wang, Z.; Li, K.; Zhang, C. Study on Coal Pillar Size Design Based on Non-integral Contact Structure of Coal and Rock Under Static and Dynamic Loads. *Front. Mater.* **2021**, *8*, 721713. [CrossRef]
9. Chen, Z.; Li, Y.; Yang, R.; Zhu, Y.; Lin, H.; Xiao, C. Non-uniform deformation mechanism and support technology of narrow coal pillar roadway. *J. China Coal Soc.* **2018**, *43*, 1847–1857.
10. Zhu, Y.; Yang, K.; Li, Y.L. Stability analysis and control strategy of layered floor of mining roadway under different coal pillar size. *J. Min. Saf. Eng.* **2023**, *40*, 467–479.
11. Zhang, M.; Wei, K.; Nian, B.; Jiang, F.; Wang, K.; Zhu, H.; Hu, H. Study on the width of section coal pillar in filling face of coal seam with rockburst hazards in deep mine. *Chin. J. Rock Mech. Eng.* **2025**, *44*, 316–330. [CrossRef]
12. Wu, C.; Wang, Z.; Liu, Y. Stability and control of surrounding rock of narrow coal pillarin vertical stratification of extra-thick coal seam. *J. China Coal Soc.* **2024**, *49*, 3728–3744.
13. Yang, K.; Gou, P. Research on Reasonable Width of Coal Pillars in High Strength Mining Roadway in Wantugou Mine. *Geotech. Geol. Eng.* **2021**, *39*, 2065–2073. [CrossRef]
14. Yu, Y.; Xie, Z.; Hu, M.; Shao, H.; Chang, S.; Bai, Y. A calculation method of reasonable size of coal pillar in large mining height section based on elastic theory. *Coal Sci. Technol.* **2023**, *51*, 37–51.
15. Dai, L.; Feng, D.; Pan, Y. Quantitative principles of dynamic interaction between rock support and surrounding rock in rockburst roadways. *Int. J. Min. Sci. Technol.* **2024**, *35*, 41–55. [CrossRef]
16. Ji, S.; Wang, Z.; Karlovsek, J. Analytical study of subcritical crack growth under mode I loading to estimate the roof durability in underground excavation. *Int. J. Min. Sci. Technol.* **2022**, *32*, 375–385. [CrossRef]
17. Ji, S.; He, H.; Karlovsek, J. Application of superposition method to study the mechanical behaviour of overlying strata in longwall mining. *Int. J. Rock Mech. Min. Sci.* **2021**, *146*, 104874. [CrossRef]
18. Cui, N.; Ma, Z.; Yang, D. Size optimization and energy analysis of coal pillar in the driving roadway along gob of the isolated coalface. *J. Min. Saf. Eng.* **2017**, *34*, 914–920.
19. Westman, E.C.; Wempen, J.M.; Coons, D.J.; McCarter, M.K.; Pariseau, W.G. Stress Redistribution in a Longwall Yield Pillar-a Comparison between Active Seismic Tomography and Theory. *Min. Metall. Explor.* **2022**, *39*, 1017–1026. [CrossRef]
20. Sherizadeh, T.; Kulatilake, P.H.S.W. Assessment of roof stability in a room and pillar coal mine in the U.S. using three-dimensional distinct element method. *Tunn. Undergr. Space Technol.* **2016**, *59*, 24–37. [CrossRef]
21. Wang, B.; Zhou, D.; Zhang, J. Research on deformation characteristics and control technology of surrounding rock for gob-side entry with small coal pillar in gently inclined coal seam. *Energy Sci. Eng.* **2024**, *12*, 1759–1774. [CrossRef]
22. Zhang, G.C.; Wen, Z.J.; Liang, S.J.; Tan, Y.L.; Tian, L.; Zhao, Y.Q.; Zhao, D.S. Ground Response of a Gob-side Entry in a Longwall Panel Extracting 17 m-Thick Coal Seam: A Case Study. *Rock Mech. Rock Eng.* **2020**, *53*, 497–516. [CrossRef]
23. Shi, J.; Feng, J.; Peng, R.; Zhu, Q. The Research on Stability of Surrounding Rock in Gob-Side Entry Driving in Deep and Thick Seam. *Geotech. Geol. Eng.* **2022**, *40*, 3357–3364. [CrossRef]
24. Wang, M.; Li, X.; Su, J.; Liu, W.; Fang, Z.; Wang, S.; Kang, J.; Yu, W. A study on the reasonable width of narrow coal pillars in the section of hard primary roof hewing along the air excavation roadway. *Energy Sci. Eng.* **2024**, *12*, 2746–2765. [CrossRef]
25. Zhao, P.; Li, G.; Li, S. Analysis of size effect of mechanical characteristics of coal pillars gob-side entry in inclined thick coal seam. *Energy Sci. Eng.* **2019**, *36*, 1120–1127.
26. Donovan, J.G.; Karfakis, M.G. Design of backfilled thin-seam coal pillars using earth pressure theory. *Geotech. Geol. Eng.* **2004**, *22*, 627–642. [CrossRef]
27. Ji, S.; Lai, X.; Cui, F.; Liu, Y.; Pan, R.; Karlovšek, J. The failure of edge-cracked hard roof in underground mining: An analytical study. *Int. J. Rock Mech. Min. Sci.* **2024**, *183*, 105934. [CrossRef]
28. Ji, S.; Karlovsek, J. Optimized differential evolution algorithm for solving DEM material calibration problem. *Eng. Comput.* **2023**, *39*, 2001–2006. [CrossRef]
29. Yoon, J. Application of experimental design and optimization to PFC model calibration in uniaxial compression simulation. *Int. J. Rock Mech. Min. Sci.* **2007**, *44*, 871–889. [CrossRef]
30. Ji, S.; Karlovsek, J. Calibration and uniqueness analysis of microparameters for DEM cohesive granular material. *Int. J. Min. Sci. Technol.* **2022**, *32*, 121–136. [CrossRef]

Disclaimer/Publisher's Note: The statements, opinions and data contained in all publications are solely those of the individual author(s) and contributor(s) and not of MDPI and/or the editor(s). MDPI and/or the editor(s) disclaim responsibility for any injury to people or property resulting from any ideas, methods, instructions or products referred to in the content.